Assessment of U.S. Urban Surface Temperature Using *GOES-16* and *GOES-17* Data: Urban Heat Island and Temperature Inequality

JANGHO LEE[a]

[a] *Department of Earth and Environmental Sciences, University of Illinois Chicago, Chicago, Illinois*

(Manuscript received 7 November 2023, in final form 11 March 2024, accepted 18 March 2024)

ABSTRACT: This study utilizes hourly land surface temperature (LST) data from the Geostationary Operational Environmental Satellite (GOES) to analyze the seasonal and diurnal characteristics of surface urban heat island intensity (SUHII) across 120 largest U.S. cities and their surroundings. Distinct patterns emerge in the classification of seasonal daytime SUHII and nighttime SUHII. Specifically, the enhanced vegetation index (EVI) and albedo (ALB) play pivotal roles in influencing these temperature variations. The diurnal cycle of SUHII further reveals different trends, suggesting that climate conditions, urban and nonurban land covers, and anthropogenic activities during nighttime hours affect SUHII peaks. Exploring intracity LST dynamics, the study reveals a significant correlation between urban intensity (UI) and LST, with LST rising as UI increases. Notably, populations identified as more vulnerable by the social vulnerability index (SVI) are found in high UI regions. This results in discernible LST inequality, where the more vulnerable communities are under higher LST conditions, possibly leading to higher heat exposure. This comprehensive study accentuates the significance of tailoring city-specific climate change mitigation strategies, illuminating LST variations and their intertwined societal implications.

KEYWORDS: Remote sensing; Social science; Urban meteorology; Societal impacts; Climate services

1. Introduction

As over 80% of the U.S. population resides in urban locales, a detailed understanding of urban temperatures becomes crucial within the context of climate impact assessments. The urban heat island (UHI) effect, a phenomenon where urban regions exhibit higher temperatures than their rural counterparts, is a pivotal factor in determining urban temperature and has profound societal and infrastructural impacts (Santágata et al. 2017; Stone et al. 2021).

UHIs are generally categorized into two types: canopy urban heat islands (CUHIs), which are derived from canopy-layer air temperature, and surface urban heat islands (SUHIs), which are based on surface temperature measurements. To measure CUHI, methods such as station observations (Beck et al. 2018) or mobile measurements (Leconte et al. 2015) have been extensively utilized. However, these methods come with their own set of limitations. Station observations, for instance, often suffer from inadequate spatial coverage, failing to comprehensively capture the temperature variations across an entire urban area. Conversely, mobile measurements, while offering more spatial flexibility, are not frequently conducted due to the considerable manpower and financial resources required.

On the other hand, SUHI is predominantly assessed using remote sensing techniques, including satellite observations. This approach has been the focal point of numerous studies (de Almeida et al. 2021; Deilami et al. 2018; Li et al. 2020; Rasul et al. 2017; Shi et al. 2021), although it is worth noting that SUHI assessments can be sensitive to the choice of dataset, methodologies, and underlying assumptions (Chakraborty et al. 2021; Hu and Brunsell 2013; Yao et al. 2018). In this study, the primary focus is on SUHI, using satellite-based estimates of land surface temperature (LST).

Research on SUHI includes extensive work on the factors driving SUHI, which is primarily attributed to differences in the energy balance between urban and nonurban areas (Manoli et al. 2020; Oke et al. 2017). Key factors influencing this energy balance disparity include variations in land cover (Li et al. 2020b; Morabito et al. 2021; Sarif et al. 2020) and anthropogenic heat release (Jin et al. 2020; Zhou et al. 2014). Previous studies also concluded that SUHI has profound societal and infrastructural impacts (Santágata et al. 2017; Stone et al. 2021). Considering that SUHI can differ greatly from city to city due to different factors, including, but not limited to, climate conditions (Lai et al. 2021; Li et al. 2020a; Shao et al. 2023) or urban morphology (Huang and Wang 2019; Zhou et al. 2022), efforts to mitigate the impact of SUHI require city-specific or even neighborhood-specific assessments that consider local climate, land use, and demographic imprints on SUHI. Ultimately, mitigation strategies need to be tailored to individual cities in ways that consider their specific contexts.

While prior research has sought to evaluate multiple cities across both global (Bechtel et al. 2019; Liu et al. 2022) and regional (Bechtel et al. 2019; Tetali et al. 2022) scales to analyze factors influencing SUHI, these expansive studies have not fully utilized the capabilities of geostationary satellites.

Denotes content that is immediately available upon publication as open access.

Supplemental information related to this paper is available at the Journals Online website: https://doi.org/10.1175/WCAS-D-23-0129.s1.

Corresponding author: Jangho Lee, jholee@uic.edu

DOI: 10.1175/WCAS-D-23-0129.1

The launch of the Geostationary Operational Environmental Satellite (*GOES-16* and *GOES-17*, hereafter referred to collectively as GOES) series opened possibilities for detailed temperature analyses across the United States (Chang et al. 2021; Lee and Dessler 2024; Li et al. 2021; Yu et al. 2008; Zhang and Du 2022). The GOES satellites, with their capability for hourly data acquisition, provide continuous observation of LST. This feature is important to ensure that short-lived, intense events do not go unnoticed. On the other hand, polar-orbiting satellites, such as MODIS (Sidiqui et al. 2016; Tomlinson et al. 2012) or Landsat (Kaplan et al. 2018; Sagris and Sepp 2017), have comparatively longer revisit periods. To address this shortcoming of infrequent LST estimates from polar-orbiting satellites, researchers often use gap-filling techniques (X. Li et al. 2018; Sarafanov et al. 2020; Shiff et al. 2021). However, employing such methods in urban environments demands a more profound comprehension of the city's energy budget, as they come with their intrinsic challenges such as anthropogenic heat release (Jin et al. 2020; Wang et al. 2021; Yuan et al. 2022), materials of buildings (Farhadi et al. 2019; Subramanian 2023), or urban morphology (Huang and Wang 2019; Zhou et al. 2022). In recognizing these limitations, I use continuous hourly LST data offered by GOES to analyze both the seasonal and diurnal characteristics of SUHI across the 120 largest U.S. cities.

While traditional work on SUHI focuses on the LST disparity between urban and nonurban areas, recent work has also emphasized the importance of intracity SUHI dynamics. These detailed spatial analyses are particularly critical in the context of temperature inequality within cities. This phenomenon can manifest in situations where populations who are less equipped to cope with extreme heat find themselves disproportionately exposed to such conditions. Previous studies analyzed intracity LST variations (Chang et al. 2022; Mentaschi et al. 2022; Yin et al. 2023; Yuan et al. 2023), pinpointing that features such as green spaces or water bodies significantly influence intracity LST. Moreover, disparities in thermal comfort across major cities have been highlighted in past research (Hsu et al. 2021; Wong et al. 2016; Wu et al. 2023). In the present study, I utilize the social vulnerability index (SVI) along with population data and high-resolution GOES LST data to provide a detailed examination of both intracity LST variations and the associated social inequalities.

2. Data

a. Selection of major U.S. cities

A total of 120 major cities and their surroundings within the United States are selected as the focal regions for this study, with the selection based on population. In assessing the climate of these cities and their nearby surroundings, substantial surrounding areas are extracted for each city. In situations where cities are too close and their surrounding territories overlap (e.g., Dallas, Texas, and Fort Worth, Texas), they are merged into a single study region. A total of 120 cities encapsulate an estimated population of 206 million, distributed across a total area of 131 000 km^2. This captures 62% of the entire U.S. population while only accounting for 1.3% of the national land area. The example of perimeters extracted in the six largest cities can be found in Figs. 1a–f, while the perimeters for the rest of the cities can be found in section S1 in the online supplemental material.

b. Land-cover data

I use land-cover data from the European Space Agency's (ESA) World Cover 2020 dataset (Zanaga et al. 2022). This dataset, originating from the Sentinel-1 and Sentinel-2 satellite constellations, provides a high-resolution view at 10 m and includes 11 generic land surface classes: tree cover, shrubland, grassland, cropland, built-up areas, bare/sparse vegetation, snow/ice, permanent water bodies, herbaceous wetland, mangrove, and moss/lichen. To harmonize these data with other products utilized here, I adjust these data to 0.01° × 0.01° latitude–longitude grids. For each of these grid cells, the encompassed land-cover types within a 0.005° radius of the grid's center are identified. Following this, I calculate the proportion of each land-cover class within each boundary. The predominant land cover, determined by the greatest representation of a land-use type, then stands as the representative land-cover type for that 0.01° grid. Figures 1a–f show the representative land cover surrounding the six largest cities in the analysis, whereas the coverage for all 120 cities and the number of pixels used are detailed in section S1.

Given the fine resolution of the land-cover data, minor segments of built-up areas surrounded by expansive non-built-up regions are observed, as shown in Figs. 1a–f. These small segments are unlikely to be classified as urban territories. On the other hand, areas of non-built-up terrain enclosed by urban regions are also noticeable. To accommodate the variances and refine urban boundaries, I employ Gaussian smoothing. The mathematical expression of Gaussian smoothing is as Eq. (1):

$$G(x, y) = \frac{e^{-(x^2+y^2/2\sigma^2)}}{2\pi\sigma^2}. \quad (1)$$

Here, x and y represent the distance from the origin in the horizontal and vertical axes, which can be referred to as latitude and longitude coordinates in this case. The term $G(x, y)$ is the Gaussian function, and σ is the standard deviation of the Gaussian distribution, which controls the magnitude of the smoothing.

To implement Gaussian smoothing, I modify the land-cover map by designating urban pixels with a value of 1 and nonurban pixels with 0, creating a binary map. On this map, I apply Gaussian smoothing using a σ value of 1, a decision reached through trial and error to achieve the most reasonable smoothing outcome. This Gaussian smoothing preserves the structure of dense urban areas, where clusters of urban pixels largely retain their original state. On the other hand, isolated urban pixels experience a decrease in value. I establish a threshold of 0.5 to smooth out these diminished urban segments. In contrast, solitary nonurban pixels that gain a value above 0.5 after smoothing, owing to their proximity to urban regions, are reclassified as urban. This method effectively smooths minor

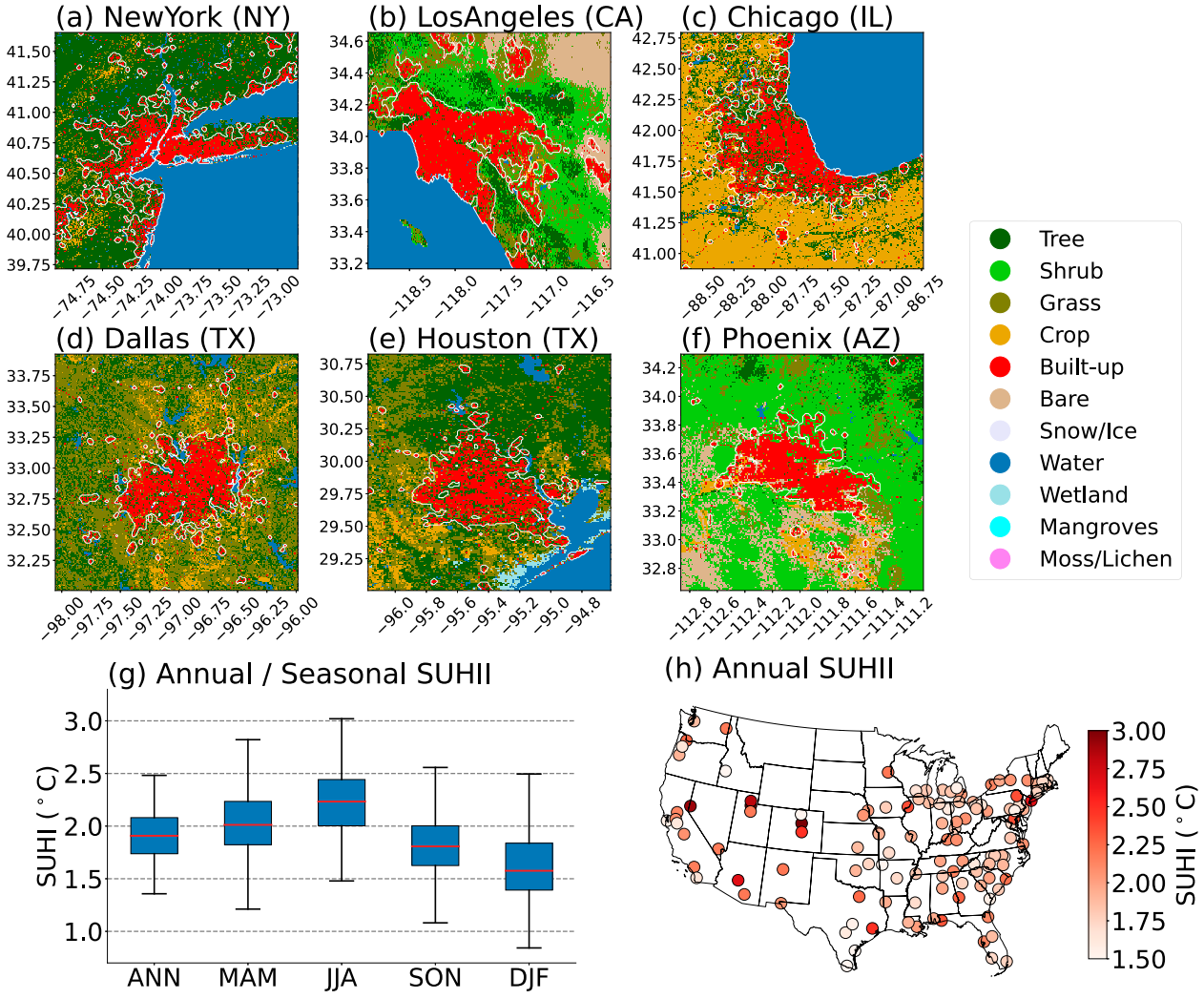

FIG. 1. (a)–(f) Land cover of the six largest cities analyzed. The white line delineates the boundary between urban and nonurban areas, determined by applying a Gaussian smoothing. (g) Distribution of annual and seasonal SUHII across all 120 cities. In the boxplot, the central box spans the interquartile range (from the 25th percentile to the 75th percentile). Whiskers extend up to 1.5 times this range, and median values are marked with red lines. (h) A spatial depiction of the cities with their corresponding annual mean SUHII values.

inconsistencies between built-up and non-built-up areas, leading to a more generalized representation of urban boundaries.

Hereafter, regions bounded by these Gaussian-smoothed demarcations are termed "urban areas," while their counterparts are labeled "nonurban areas." Importantly, both classifications exclude water bodies, ensuring neither urban categories nor nonurban categories comprise any permanent water features. The extent of urban and nonurban areas of interest is visually represented in Figs. 1a–f as well as in Fig. S1. Across all cities, the average ratio of urban to nonurban pixels is 0.29. For a comprehensive breakdown of the number of urban and nonurban pixels utilized in this study, refer to Table S1.

It should be noted that in certain cases, such as Los Angeles, California, as depicted in Fig. 1b, urban areas that could be perceived as separate from the designated city region may be encompassed in the study (e.g., the patch of urban areas in the northeast of Los Angeles). Therefore, it is essential to view the outcomes of this study not as specific to the exact boundaries of individual cities, but rather as results that consider a broader perspective, including the 120 major cities in the United States and the potential inclusion of their surrounding urban areas.

c. GOES-16/17 *data*

The LST data in this study come from the GOES LST data (Yu and Yu 2020). The LST data used here cover the contiguous United States (CONUS) for 5 years, from 2018 to 2022. They are collected every hour and have a 2-km spatial resolution, which is about 0.02° latitude–longitude at the equator. Because the LST data are on an irregular grid, they are changed to fit a 0.01° regular grid, to match the land-cover dataset. For this change, the nearest neighbor method is used to preserve all the information of GOES data by oversampling. The inheriting limitation of the satellite data is that they

cannot measure temperatures under clouds. To address this, I use a cloud mask product from GOES to remove data from cloudy areas. Thus, the LST data used in this study can be viewed as cloud-free hourly LST data for each city.

d. Auxiliary data

To get a clearer picture of the atmospheric and climate conditions for each city, the ERA5 Land monthly dataset (Muñoz-Sabater et al. 2021) is used. This dataset is on a 0.1° grid and provides monthly averages of 2-m air temperature (T2M) and 2-m dewpoint temperature (D2M) for the cities and the surroundings. Using T2M and D2M data, I also calculate the surface relative humidity (RH). It should be noted that the ERA5 dataset does not explicitly account for urban area effects.

Furthermore, the enhanced vegetation index (EVI, VNP13A3) data, obtained from the Visible Infrared Imaging Radiometer Suite (VIIRS), is used as a metric for vegetation. Although other metrics, such as the normalized difference vegetation index (NDVI) or the leaf area index (LAI), are available, the choice of EVI is based on the observation that different indices do not significantly alter the overall study results. Additionally, two other VIIRS datasets were utilized: albedo (ALB, VNP43MA3) and nighttime light (NL, VNP46A3). These datasets were originally in a 1-km irregular grid format but were regridded to a 0.01° regular grid using the same methodology applied to the GOES LST data. I calculate the differences between urban and nonurban values for EVI, ALB, and NL, referred to as ΔEVI, ΔALB, and ΔNL, respectively. While EVI is a monthly product, ALB and NL are available daily. To ensure uniformity across all data types, monthly averages were computed for ALB and NL.

e. Population and social vulnerability index

The Gridded Population of the World Version 4 (GPW v4) dataset is used for the population data (Doxsey-Whitfield et al. 2015). This dataset presents data in 30-arc-s latitude–longitude grids. To align the population data with other datasets, I aggregate the data into a 0.01° regular grid. First, I assign each grid cell in the population dataset to its nearest point on the 0.01° regular grid. At each of these 0.01° grid points, the populations of all assigned grid cells are summed, allowing for the transposition of the population data onto a 0.01° regular grid without changing the total population count.

I also integrate the gridded SVI for socioeconomic insights (Flanagan et al. 2011). The gridded SVI product encompasses various subcategories, such as socioeconomic status, household composition, disability, minority status, language, housing type, and transportation. SVI is initially at the census tract level. However, for this study, I utilize SVI data that have been regridded to a 1-km resolution by the Socioeconomic Data and Applications Center (SEDAC). These regridded SVI data are available for the years 2000, 2010, 2014, 2016, and 2018. I use 1-km resolution SVI data from 2018, as they align most closely with the study period (2018–22). SVI values can vary between 0 and 1, with 1 pointing to the most vulnerable population segments. SVI values are originally in 1-km resolution, so I also adjust these data to the 0.01° regular grid, using an approach like that of the population dataset, but values are averaged instead of summed.

All data used in this study are summarized in section S2, including source, resolution, and processing method.

3. Method of analysis

a. Surface urban heat island

A crucial factor in analyzing urban temperature is the SUHI effect. The SUHI intensity (SUHII) represents the temperature difference between urban and nonurban areas. To determine this, the mean temperature within urban boundaries is calculated hourly. The difference between this and the hourly mean temperature in nonurban regions yields the hourly SUHII. Due to occasional observation limitations in GOES LST caused by cloud cover, hours with more than 50% cloud cover over urban or nonurban regions are excluded. This process yields a city-specific cloud-free SUHII time series with hourly intervals, spanning 5 years (2018–22).

Initially, the overall SUHII is determined for each city by averaging all SUHII time-series values. Subsequently, SUHII is computed seasonally, divided as follows: March–May (MAM), June–August (JJA), September–November (SON), and December–February (DJF). Mathematically, this can be expressed as Eq. (2), where s represents each season (MAM, JJA, SON, and DJF):

$$\mathrm{SUHII}(s) = \overline{\mathrm{LST}_{\mathrm{urban}}(s)} - \overline{\mathrm{LST}_{\mathrm{nonurban}}(s)}. \quad (2)$$

Throughout the research period, the mean SUHII across all cities is 1.9°C. As depicted in Fig. 1g, the JJA season shows the highest average SUHII across all cities at 2.2°C. Figure 1f presents the spatial distribution of the annual SUHII for each city. Across all 120 cities and seasons, SUHII consistently displays positive values for all cities and seasons. The only exception is San Diego, California, during the JJA season, where the SUHII registers at −0.2°C.

The increased LST in urban areas is primarily attributed to differences in land cover between urban and nonurban areas, as established in numerous previous studies (Bechtel et al. 2019; Peng et al. 2018; Rousta et al. 2018; Yao et al. 2019). In the analysis of 120 cities in this study, the average surrounding land cover consists of 51% trees, 22% grass, and 17% croplands. Notably, the presence of trees and grass significantly contributes to the reduction in LST, thereby playing a crucial role in the SUHI effect (Bindajam et al. 2020; Guha and Govil 2022; Rogan et al. 2013; Yang and Yao 2022).

b. Seasonal and diurnal SUHI cycles

Delving deeper into the details of SUHII and its seasonal variations, a monthly average for each city is derived from the 5-yr hourly SUHII data. Given that daytime SUHII and nighttime SUHII exhibit different characteristics (Chakraborty et al. 2020; Liu et al. 2022; Rasul et al. 2016), two distinct monthly averages are determined: one for daytime SUHII and another for nighttime SUHII. Hourly SUHII values are classified as day or night for each day based on the calculated sunrise and

sunset times specific to each city and date. From these classifications, monthly average values for both daytime SUHII and nighttime SUHII are obtained. Mathematically, the seasonal cycle of SUHII for daytime and nighttime can be expressed as Eqs. (3) and (4):

$$\text{Seasonal}_{\text{daytime}}(m, C) = \frac{\sum_{y=1}^{5} \sum_{h=1}^{N_{\text{dm},m,y}(C)} \text{SUHII}_{\text{daytime}}(h, m, y, C)}{\sum_{y=1}^{5} N_{\text{dm},m,y}(C)}, \tag{3}$$

$$\text{Seasonal}_{\text{nighttime}}(m, C) = \frac{\sum_{y=1}^{5} \sum_{h=1}^{N_{\text{nm},m,y}(C)} \text{SUHII}_{\text{nighttime}}(h, m, y, C)}{\sum_{y=1}^{5} N_{\text{nm},m,y}(C)}. \tag{4}$$

In Eqs. (3) and (4), $\text{Seasonal}_{\text{daytime}}(m, C)$ and $\text{Seasonal}_{\text{nighttime}}(m, C)$ each represent the seasonal cycles of daytime SUHII and nighttime SUHII, at month m and city C. In Eq. (3), $\text{SUHII}_{\text{daytime}}(h, m, y, C)$ is the daytime SUHII value for a given daytime hour h, month m, and year y for city C. The term $N_{\text{dm},m,y}(C)$ is the number of daytime hours in month m of year y for city C. The same convention is used in Eq. (4), but for nighttime, where $\text{SUHII}_{\text{daytime}}(h, m, y, C)$ is the nighttime SUHII value and $N_{\text{nm},m,y}(C)$ is the number of nighttime hours.

A similar approach is also applied to diurnal variations of SUHI by averaging SUHII for each hour of the day across the entire study period. The mathematical expression for calculating the diurnal SUHI cycle can be represented as Eq. (5):

$$\text{Diurnal}(h, C) = \frac{\sum_{y=1}^{5} \sum_{m=1}^{12} \sum_{d=1}^{D_m} \text{SUHII}(h, d, m, y, C)}{\sum_{y=1}^{5} \sum_{m=1}^{12} D_m}. \tag{5}$$

In Eq. (5), the $\text{Diurnal}(h, C)$ represents the average SUHII for a given hour h across all cities denoted by C. The numerator aggregates the hourly SUHII values $\text{SUHII}(h, d, m, y, C)$, which are specific to each city C for each hour h, day d, month m, and year y across the 5-yr study period. The term D_m corresponds to the number of days in each month m. The denominator divides the sum of SUHII values by the total number of hours that contribute to the dataset, resulting in an average that encapsulates the diurnal variation of SUHII.

c. *k-means clustering*

For each of the two seasonal cycles (daytime and nighttime), cities show similarities and disparities. To analyze both shared and unique patterns of seasonal SUHII variation across cities, I utilize k-means clustering. The initial step in the clustering process involves normalizing 120 city-specific, 12-month time series. Each city's seasonal SUHII cycle is normalized by subtracting the mean and dividing by the standard deviation, which allows us to focus on the relative shape of the cycles, not the absolute magnitude.

To further refine the analysis, I embed a 1-month lag into each time series to adjust for potential phase shifts between the cycles. This embedding is essential for synchronizing cycles that may differ by a 1-month offset, thereby allowing the clustering algorithm to more accurately group cities with synchronized SUHII patterns. In mathematical terms, for a given time series t_s of length 12 (monthly time series), the embedding translates into constructing a new matrix where each row is formed by pairing the original time series with its 1-month lagged sequence. Consequently, the resulting matrix for each city's seasonal cycle is an 11×2 array, where one column is the original time series, and the other is its 1-month lagged counterpart.

Finally, I use the k-means clustering method for each of the seasonal cycles. Mathematically, this can be achieved by solving the optimization problem as in Eq. (6):

$$\text{minimize} : \sum_{j=1}^{k} \sum_{i \in S_j} \|X_i' - \mu_j\|^2. \tag{6}$$

In Eq. (6), X_i' represents the ith embedded time series after applying a 1-month lag, S_j is the set of indices of the time series belonging to the jth cluster, and μ_j is the centroid of the jth cluster.

A similar calculation is done for the diurnal cycle, with the difference being the length of each time series being 24 h, rather than 12 months, and the lag being 1 h, rather than 1 month. The number of clusters k is selected using the silhouette score and is determined at 3 for seasonal daytime, 2 for seasonal nighttime SUHII, and 2 for diurnal SUHII. Details on calculating the optimal number of clusters can be found in section S3.

4. Seasonal and diurnal SUHI cycles

a. *Daytime SUHII seasonal cycle*

Figure 2 depicts the description of the daytime SUHII seasonal cycle. The assigned cluster for each city and the proportional distribution of clusters are illustrated in Figs. 2a and 2b, respectively. In Fig. 2c, the normalized mean of the daytime seasonal SUHII cycle for cities in cluster 1 is presented. SUHII values are normalized to address the varying intensities across cities, simplifying the process of identifying the general pattern of the seasonal cycle. Given that 67% of the cities fall within cluster 1, this pattern can be regarded as typical of the daytime seasonal cycle of SUHII. The land covers surrounding these cities are detailed in Fig. 2d. The seasonal cycles of RH—using monthly averages from both urban and nonurban areas—nonurban EVI, and normalized ΔEVI are displayed in Figs. 2e–g.

The second most common SUHII pattern is captured by cluster 2 (21%) as shown in Fig. 2h. The cities that fall within this cluster show the daytime seasonal cycle of SUHII that includes a pronounced decline during the late spring and early

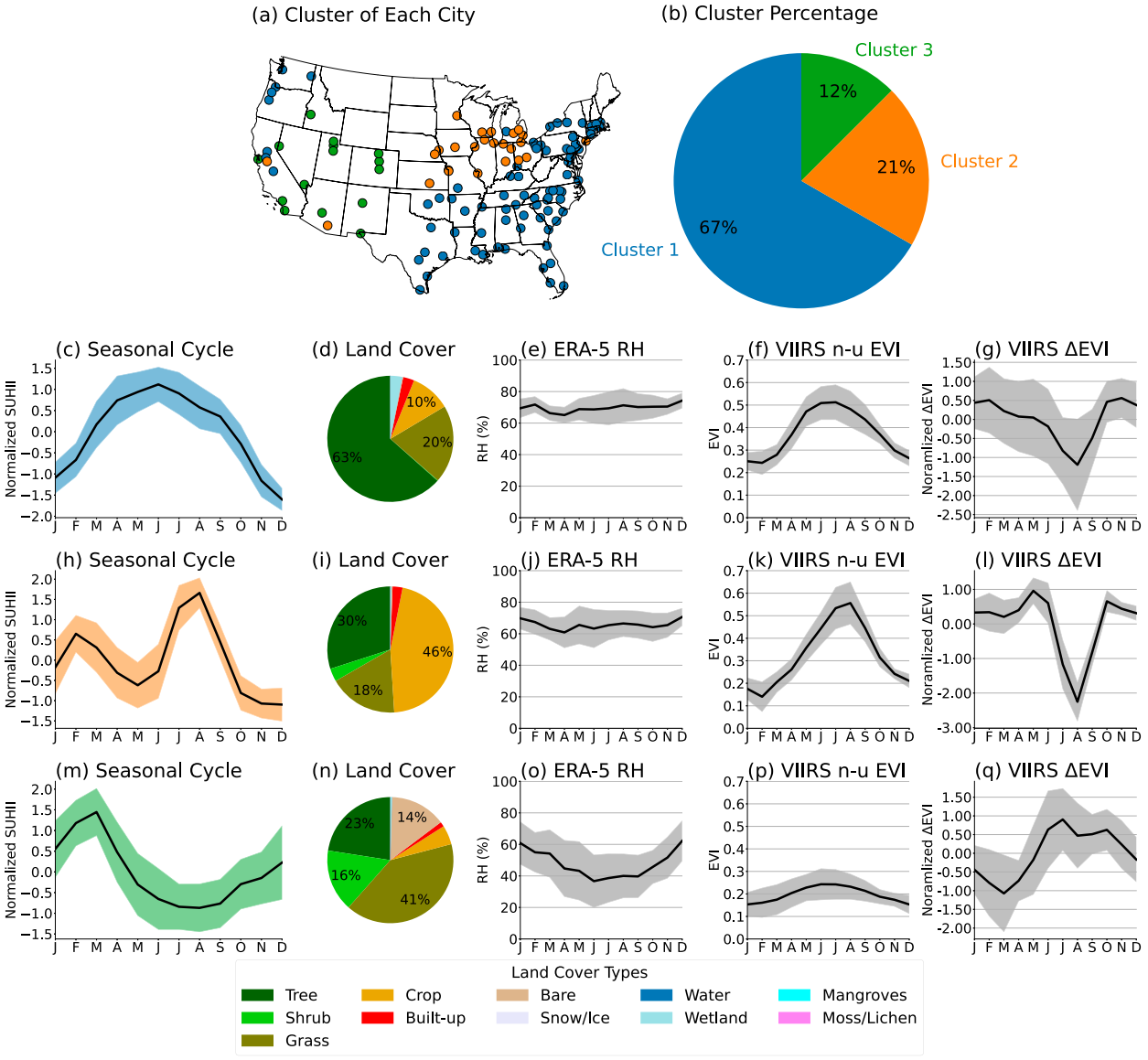

FIG. 2. (a) Clusters assigned to each of the 120 cities in this study, based on daytime seasonal SUHII patterns. (b) Proportional representation of each cluster. (c) Daytime seasonal cycle of normalized SUHII for cities within cluster 1. The black line represents the average, while the shaded area indicates the one standard deviation range. (d) Nonurban land covers associated with the cities in cluster 1. Percentages of each land-cover type are determined for every city and then averaged to display the composite value. (e) The seasonal cycle of RH in cities is categorized under cluster 1. Both urban and nonurban RH estimates contribute to the mean values. The black line signifies the average, with the shaded area marking the one standard deviation range. (f) As in (e), but for nonurban EVI. (g) As in (e), but for normalized ΔEVI. (h)–(l) As in (c)–(g), but for cluster 2. (m)–(q) As in (c)–(g), but for cluster 3.

summer months (April–June). The cause for this pattern may be that these cities are more commonly surrounded by croplands, constituting 46%, surrounding the cities in cluster 2, as illustrated in Fig. 2i. Previous studies found that croplands typically exhibit higher LST than other natural land covers, particularly in the spring season prior to planting (Ramankutty et al. 2006; Y.-C. Wang et al. 2018; Wickham et al. 2012), and this high LST of croplands tends to decrease in the fall season, when vegetation of croplands increases (Shen et al. 2018; Yang et al. 2020). Elevated LST in croplands results in a lower LST difference between urban and nonurban regions, leading to a reduction in SUHII in the spring season, as evidenced in Fig. 2h. Moreover, an increase in nonurban EVI (Fig. 2k) and a decrease in ΔEVI (Fig. 2l) drive the SUHII peak in August, depicted in Fig. 2h. Given that an elevated EVI is associated with cooler LST, it is expected that a higher ΔEVI would decrease daytime SUHII. In line with this expectation, the patterns in Figs. 2h and 2l appear inversely related, offering clarity on the daytime SUHII behavior in cluster 2.

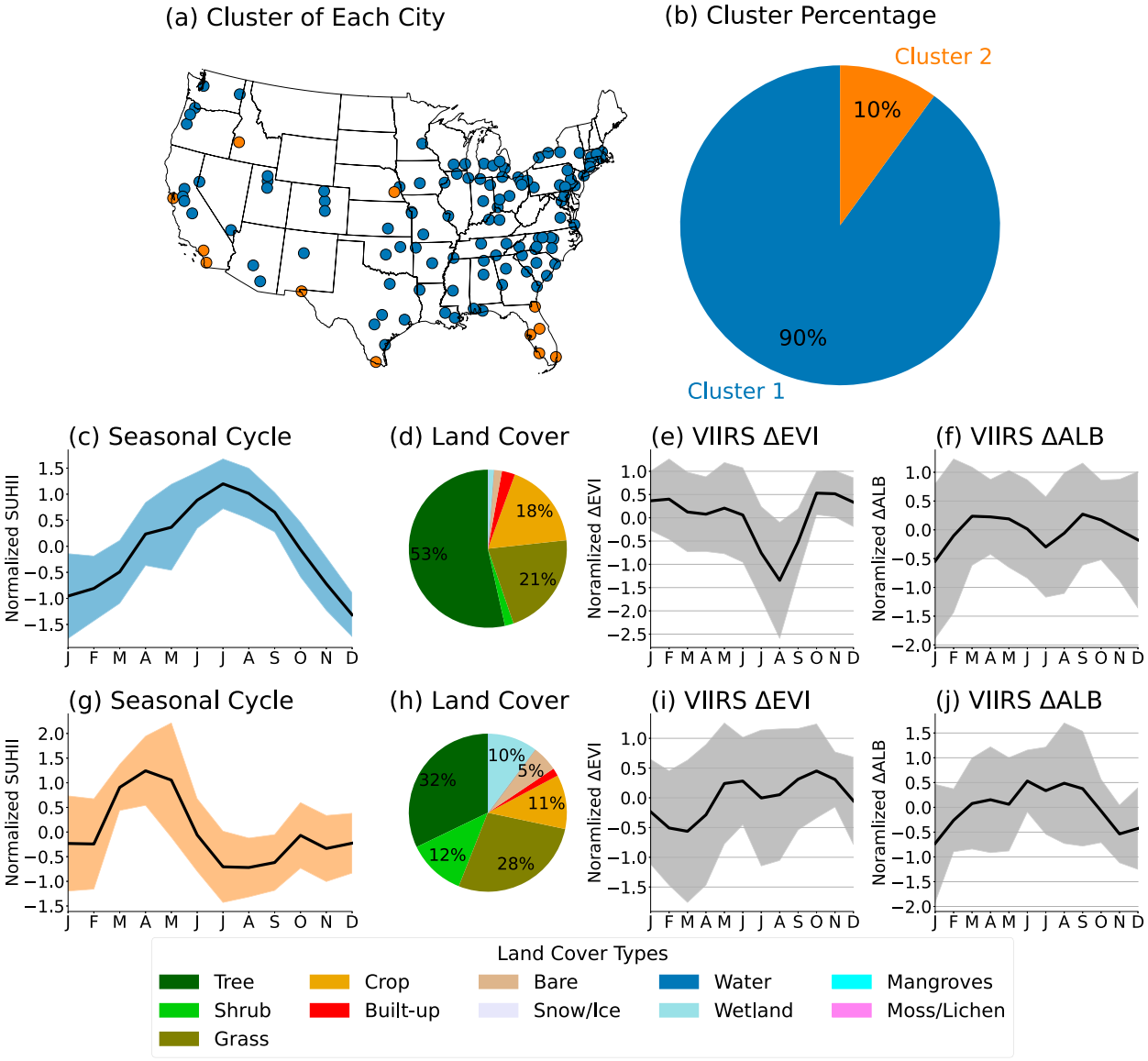

FIG. 3. (a) Clusters assigned to each of the 120 cities in this study, based on nighttime seasonal SUHII patterns. (b) Proportional representation of each cluster. (c) The nighttime seasonal cycle of normalized SUHII for cities within cluster 1. The black line represents the average, while the shaded area indicates the one standard deviation range. (d) Nonurban land covers associated with the cities in cluster 1. Percentages of each land-cover type are determined for every city and then averaged to display the composite value. (e) The seasonal cycle of ΔEVI in cities categorized under cluster 1. The values of ΔEVI are normalized for each city. The black line signifies the average, with the shaded area marking the one standard deviation range. (f) As in (e), but for normalized ΔALB. (g)–(j) As in (c)–(f), but for cluster 2.

Cities within cluster 3 (12%) are characterized by their arid climate, as indicated by low RH values shown in Fig. 2o, and a predominance of grass and bare land covers surrounding the cities, as delineated in Fig. 2n. Furthermore, a notably lower EVI is observed in cities in cluster 3 in comparison with other clusters (Fig. 2p). A distinctive seasonal cycle of ΔEVI, peaking in summer, is seen in these cities, which explains the pattern of seasonal SUHII in cluster 3. This pattern of seasonal cycle in arid cities is also reported in the previous study (Liu et al. 2022). In summary, as observed in both cluster 2 and cluster 3, ΔEVI is identified as a primary factor influencing the daytime seasonal SUHII. Quantitatively, the average correlation coefficient between seasonal SUHII and ΔEVI for all cities is −0.51.

b. Nighttime SUHII seasonal cycle

Nighttime seasonal SUHII is classified into two clusters, as illustrated in Fig. 3. Most cities fall under cluster 1, while only 10% are categorized into cluster 2 (Figs. 3a,b). A significant difference between clusters 1 and 2 is the reduction in nighttime SUHII during the summer months (Figs. 3c,g). Several potential factors can contribute to the inverse seasonal pattern

between the cities in clusters 1 and 2. First, the role of ΔEVI is possible. As discussed in the previous section, ΔEVI is inversely correlated with SUHII. This correlation clarifies the elevated levels of SUHII in the spring season for cluster 2, when ΔEVI is lower. Additionally, the notable summer decrease in ΔEVI observed in cluster 1 is less prominent in cluster 2, accounting for the summertime disparity in SUHII in clusters 1 and 2.

Another possible influential variable is ΔALB, known to be a significant determinant of nighttime SUHI. Previous studies indicate that higher ΔALB values generally correspond to reduced nighttime SUHII (Dutta et al. 2022; Liu et al. 2022). The primary energy source for nighttime SUHI originates from the heat absorbed by urban environments during the day. However, when urban ALB is high, most of this energy is reflected during the daytime, leaving less residual heat to drive nighttime SUHI. The reduction in ΔALB during the summer months is shown in cluster 1 but not in cluster 2, accounting for the observed discrepancies in summertime SUHII between the two clusters.

However, the predominance of cities in cluster 1, coupled with the significant error margins in potential drivers such as ΔEVI and ΔALB, complicates the identification of specific factors influencing nighttime SUHI in cluster 2. This complexity is accentuated in the nocturnal context, where SUHI dynamics are inherently more complex than daytime, as evidenced by previous studies (El Kenawy et al. 2020; Krayenhoff et al. 2018; Leconte et al. 2020; Ming et al. 2023; Wang and Li 2017). Additionally, this study does not encompass certain mechanisms known to affect nighttime SUHI. Notably, the influence of 2D/3D urban morphology, which plays a significant role in shaping nighttime SUHI dynamics (El Kenawy et al. 2020; Peng et al. 2022; Siddiqui et al. 2021), was not examined. Furthermore, factors such as the higher thermal admittance of building materials (Oke 1982; Subramanian 2023) and the contribution of anthropogenic heat emissions (Best and Grimmond 2015; Feng et al. 2012; Ward et al. 2016) further add to the challenges in pinpointing distinct drivers of nighttime SUHI. Given the complexity of nighttime SUHI dynamics and the limitations observed in this study, it becomes evident that further research is essential to comprehensively understand and accurately identify the drivers of nighttime SUHI.

c. *Diurnal cycle of SUHII*

Leveraging the hourly LST measurements provided by GOES, I conduct a more detailed assessment of the SUHII by analyzing its diurnal cycle. The diurnal cycle of SUHII in clusters 1 and 2 shows a significant discrepancy, as cluster 1 follows the general cycle of incoming solar radiation, while cluster 2 peaks in the late evening (2000–2100 LT) and reaches its minimum in the morning (0800–0900 LT).

An examination of land cover (Figs. 4d,f), RH (Fig. 4g), and EVI (Fig. 4h) reveals that cities in cluster 2 are characterized by a more arid climate with lower humidity and reduced vegetation. Previous studies have noted that a diurnal SUHII pattern peaking at nighttime, rather than at noon, is typical for cities situated in arid climates with sparse vegetation (Liu et al. 2022; C. Wang et al. 2018; Wang et al. 2016; Wang and Li 2021). Utilizing the Kruskal–Wallis test to examine the significance of differences in RH and EVI between the two clusters, both variables are found to have statistically significant differences in their means ($P < 0.05$).

Upon analysis of ΔEVI (Fig. 4i), ΔALB (Fig. 4j), and ΔNL (Fig. 4k), all three variables are identified as statistically distinguishable between the two clusters ($P < 0.05$). Despite cluster 2 generally displaying reduced EVI (Fig. 4h), a greater ΔEVI is observed (Fig. 4i) in this cluster. This means that in such locales, the bare soils in nonurban regions heat up more quickly than those in urban areas, contributing to lower SUHII values following sunrise. This phenomenon is further substantiated by the lower ΔALB values in these cities, where high nonurban ΔALB is attributed to sparse vegetation and exposed soils. Furthermore, as low ΔALB can be translated to lower ALB in urban regions, cities with low ΔALB (cluster 2) will absorb more radiated heat during the daytime. This absorbed heat will be released slowly at nighttime, which causes the nighttime SUHII to increase, as in cluster 2.

Additionally, ΔNL is found to be considerably higher in cluster 2. The variable ΔNL serves as an indicator correlated with the urban-to-nonurban gradient of human activity or anthropogenic heat released during the nighttime. Elevated ΔNL levels indicate greater anthropogenic heat release in urban areas, consequently resulting in increased nighttime SUHII, as observed in cluster 2 (Fig. 2e). A complete figure regarding daytime seasonal SUHII, nighttime seasonal SUHII, and diurnal SUHII can be found in section S4.

5. Intracity LST and climate inequality

a. *Intracity LST by UI*

Until this point, the emphasis has been on the city scale without considering intracity LST differences. To study the intracity difference, I utilize land-cover data. In previous sections, land cover for each GOES grid point was determined using a land cover with the highest percentage within a 0.005° radius of GOES grids. However, for the analysis of intracity LST, land cover for each GOES grid point is not determined as a single representative. Instead, the percentage of built-up area within a 0.005° radius is calculated and referred to as urban intensity (UI). This metric serves to quantify each GOES grid point based on the extent of built-up areas, considering intracity variations in non-built-up areas (vegetation or water bodies). Such calculations are performed exclusively within the urban boundaries, as indicated by the white lines in Figs. 1a–f.

To assess intracity variations in LST, timestamps are initially selected where over 90% of the urban boundary is free of cloud cover. For these selected timestamps, LST anomalies are calculated. An LST anomaly at a given grid point is defined as the LST at that gridpoint time minus the average LST within the city-specific urban boundaries within the same timestamp. Thus, it indicates how much each grid point is hotter or cooler than other contemporary local urban areas.

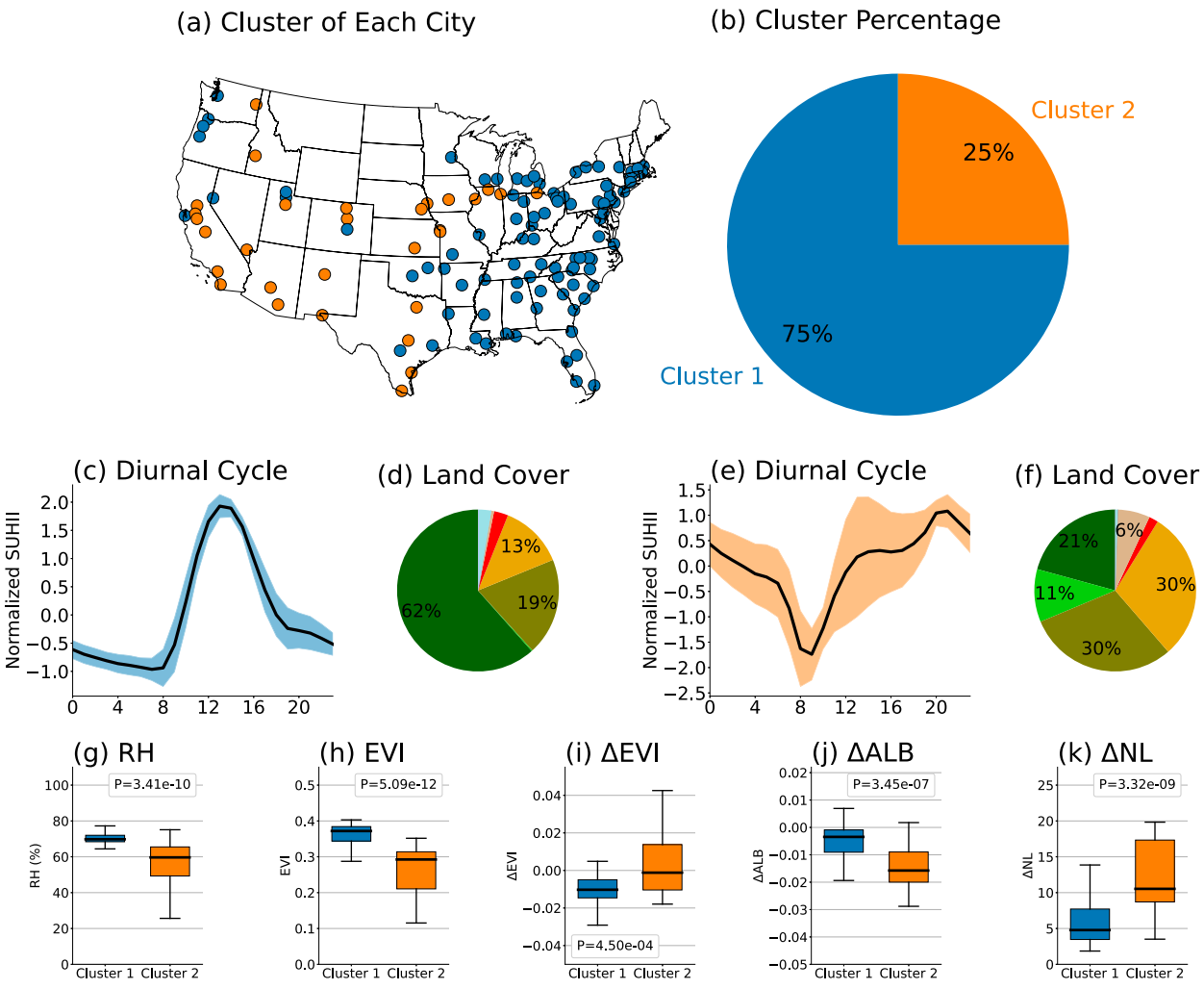

FIG. 4. (a) Clusters assigned to each of the 120 cities in this study, based on diurnal SUHII patterns. (b) Proportional representation of each cluster. (c) Diurnal cycle of normalized SUHII for cities within cluster 1. The black line represents the average, while the shaded area indicates the one standard deviation range. (d) Nonurban land covers associated with the cities in cluster 1. Percentages of each land-cover type are determined for every city and then averaged to display the composite value. (e),(f) As in (c) and (d), but for cluster 2. (g) Distribution of average RH from cluster 1 (blue) and cluster 2 (orange). In the boxplot, the central box spans the interquartile range (from the 25th percentile to the 75th percentile). Whiskers extend up to 1.5 times this range, and median values are marked with black lines. The p value from the Kruskal–Wallis test to compare the significant difference between the two samples is also denoted in the figure. (h)–(k) As in (g), but for EVI, ΔEVI, ΔALB, and ΔNL, respectively.

Figure 5a depicts the change in average LST anomaly for each 10% increment in UI. The figure illustrates a trend where LST anomaly rises as the UI escalates, meaning that at a given time, high UI grid points have higher LSTs than their lower UI counterparts. For every 10% increment in UI, the LST rises by 0.066°C. This positive correlation holds across all cities, as demonstrated in Fig. 5b.

When examining the average diurnal variation of intracity LST anomalies across the 10% UI bins (Fig. 5c), a significant LST offset is observed around early evening (1800–2000 LT) and is at its lowest around noon. This indicates that during peak solar radiation times, intracity LST variations are primarily influenced by the incoming solar radiation, thus minimizing differences due to UI. In contrast, during the evening, areas with higher UI tend to exhibit increased LSTs. This is attributed to urban materials releasing stored heat from the daytime. This trend is also consistent in all cities, as shown in Fig. 5d, where the slope of LST and UI is greatest during the evening.

b. *Social inequality*

Social inequality in thermal comfort has been an interest in previous studies (Pereira et al. 2021; Wu et al. 2023). Although a complex relationship exists between LST and thermal comfort, in a way that LST might overestimate the variability in air temperature and, consequently, in thermal comfort, it can still serve as an indirect proxy of thermal comfort (Goldblatt et al. 2021; Imran et al. 2021; Patel et al. 2024). In that context, I now compare the LST differences within cities with SVI data.

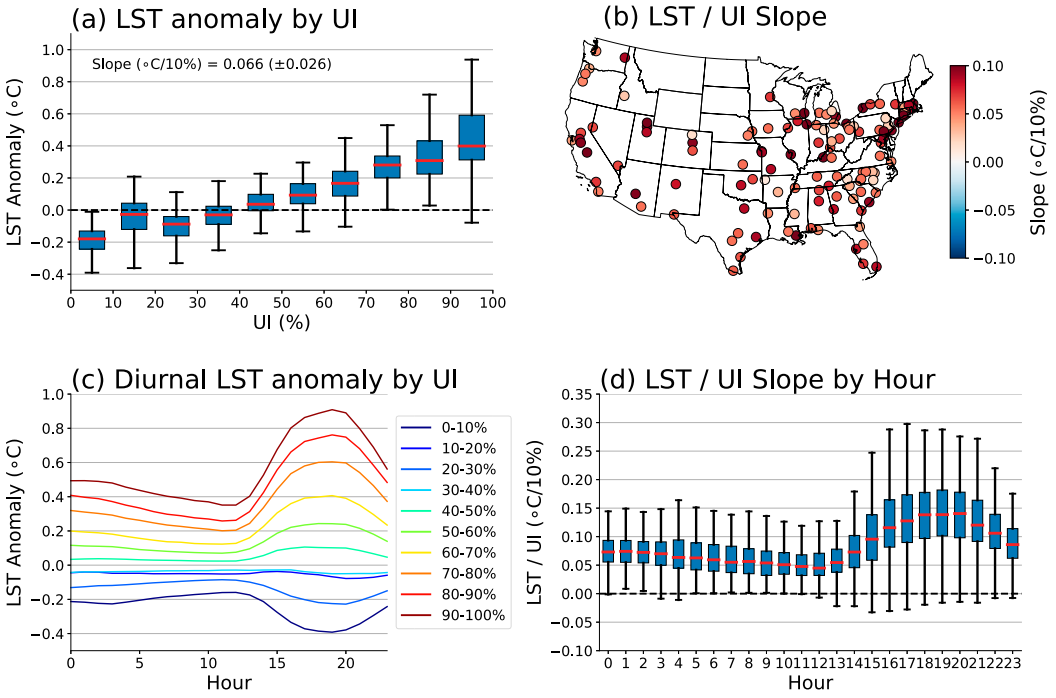

FIG. 5. (a) Boxplot of LST anomaly across each 10% UI increment. Each box denotes the distribution of LST anomaly in 120 cities in this study. In the boxplot, the central box spans the interquartile range (from the 25th percentile to the 75th percentile). Whiskers extend up to 1.5 times this range, and median values are marked with black lines. (b) Spatial distribution of the UI and LST anomaly slopes for individual cities, derived from (a). (c) Diurnal variation in LST anomaly, averaged across cities, presented for each UI bin. (d) The hourly UI–LST slope. Each box illustrates the distribution of the UI–LST slope across 120 cities, presented similarly to (a).

As in Fig. 6a, SVI tends to be positively correlated with UI, meaning that populations with high vulnerability are in intensive urban environments. This trend is true in 90% of the cities (108 out of 120 cities), and for the cities that have a negative correlation, the magnitude of the slope is small, as seen in Fig. 6b. By this, one can expect that high SVI communities would be under higher LST conditions.

To correlate SVI levels to LST, a population-weighted SVI threshold is derived. This method is adopted due to the disparate SVI ranges observed across different cities. Utilizing the gridded population dataset, an array of SVIs is constructed, where its length mirrors the population size. Each element of this array denotes the SVI for every individual within the city. Subsequently, percentile thresholds of SVI are determined in 10-percentile increments. Leveraging these thresholds, individual grid points are categorized based on their corresponding SVI percentiles. Since the focus is on the inequality of LST to different SVI levels, the average LST of the most vulnerable population segment (those over the 90th percentile of SVI) is compared to the least vulnerable segment (those below the 10th percentile of SVI) by subtracting the LST of low SVI groups from the high SVI groups, during summertime (JJA) from 1000 to 1600 LT, the peak LST period. This measure provides insight into the average LST differential between populations with high and low vulnerability during the hottest periods. This metric is subsequently referred to as the heat inequality index (HII).

Upon examination of the HII distribution across cities, it is observed that the average HII is at 0.54°C (red line in Fig. 6c). This indicates that during periods of high heat, the more vulnerable populations experience even higher LSTs, by an average of 0.54°C. Such a trend is observed in most cities, with 103 out of 120 cities exhibiting this pattern. These findings suggest that communities with more vulnerability are typically situated in areas of high urban intensity, and as a result, they face higher LSTs during the summer, averaging a difference of 0.54°C. A complete table of information regarding UI, SVI, and HII for individual cities can be found in section S5.

It is important to note that both the SVI and the UI are presented on a 0.01° × 0.01° regular grid. While this granularity might not be adequate for detailed analyses, such as examining SVI changes at the neighborhood or block level, it is important to consider the underlying data sources. SVI is derived from census tract data, and the LST product used in this study represents an average over a 2-km resolution. Consequently, the observed relationship between LST and SVI should be interpreted as indicative of general trends rather than precise local variations.

6. Summary and conclusions

Using the hourly LST measurements from GOES, I carried out an assessment of the seasonal and diurnal cycles of SUHII, as well as intracity LST variation and associated societal inequality. For the seasonal cycle of daytime SUHII, 120 cities

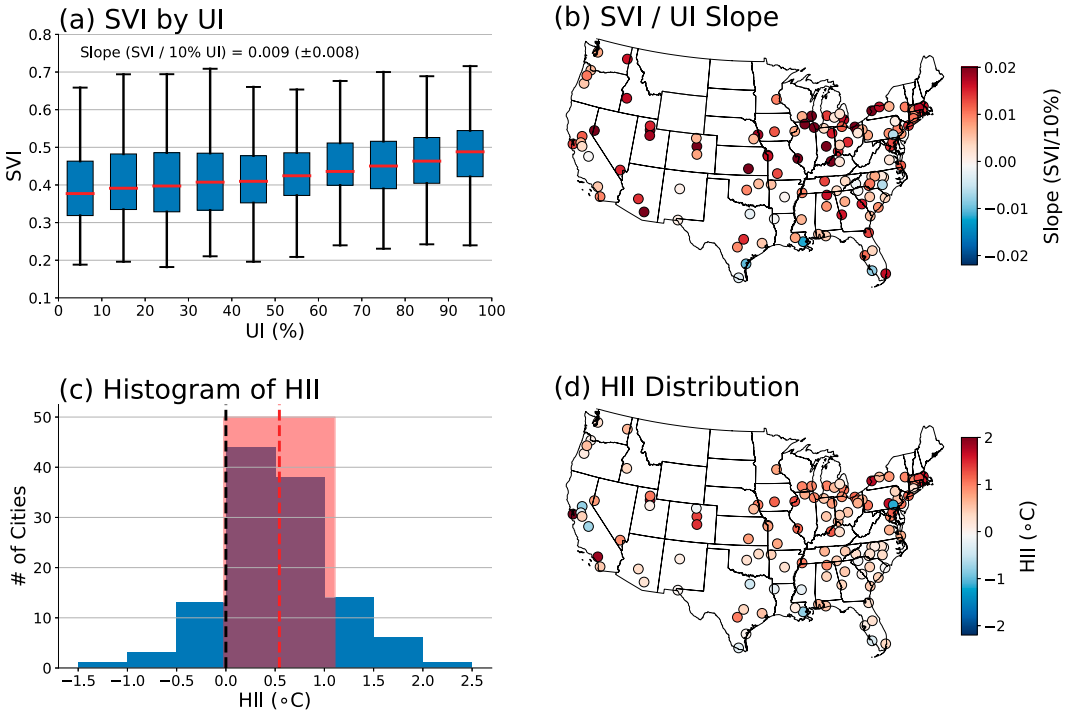

FIG. 6. (a) Boxplot of SVI across each 10% UI increment. Each box denotes the distribution of LST anomaly in 120 cities in this study. In the boxplot, the central box spans the interquartile range (from the 25th percentile to the 75th percentile). Whiskers extend up to 1.5 times this range, and median values are marked with black lines. (b) Spatial distribution of the UI SVI slope for individual cities, derived from (a). (c) Histogram of HII across all cities. The red dashed line denotes the mean, while the shaded region shows the one standard deviation range. (d) Spatial distribution of HII for individual cities, derived from (c).

are categorized into three distinct clusters, with regional EVI identified as the primary determinant of SUHI due to its capability to cool surrounding LST. The seasonal cycle of nighttime SUHII is grouped into two clusters where most of the cities are assigned to cluster 1. The mechanisms governing this are more complex. However, both EVI and ALB are determined to possibly affect the seasonal cycle of nighttime SUHII. The diurnal cycle of SUHII is divided into two clusters: The first cluster exhibits a diurnal cycle that peaks around noon, while the second cluster peaks in the evening. This variation arises from factors such as the city's humidity levels, land cover, and the extent of human activity during nighttime hours.

Looking at the intracity LST distribution, a positive correlation between intracity LST and UI was identified. Within a given city, areas with a higher proportion of built structures, as opposed to green spaces or water bodies, exhibited elevated LST. Specifically, a 0.066°C increase in LST was observed for every 10% rise in UI. Additionally, a correlation between SVI and UI was detected, with SVI increasing by 0.009 for every 10% escalation in UI. These interrelationships among UI, LST, and SVI contribute to LST inequality. The findings of this study reveal that during peak heat periods, the more vulnerable population segments experience LST that is 0.54°C warmer than their less vulnerable counterparts.

In this study, I explore LST variations across 120 U.S. cities utilizing GOES data. The unique capability of GOES satellites to provide hourly LST lends a distinct advantage and authenticity to this research. This effort to create a database of the SUHI effect on major cities in the United States is novel, as previous research used LST that is estimated once daily, or gap-filled LST estimates from polar-orbiting satellites to conduct similar research (Bechtel et al. 2019; Liu et al. 2022). Moreover, I investigate the physical mechanisms that govern the SUHII dynamics across individual cities. Recognizing unique drivers is important, as it underscores the necessity for tailored climate change mitigation strategies based on the distinctive characteristics of each city.

For example, the majority of cities belong to cluster 1 in both seasonal and diurnal cycles of SUHII—which indicates higher SUHII in summer and noon. Since this study found that ΔEVI plays a critical role in this pattern, increasing urban green spaces could significantly help mitigate SUHI in these cities. On the other hand, cities that suffer higher LST at nighttime (cluster 2 in the diurnal cycle) should minimize the impact of SUHI by decreasing nighttime activity (ΔNL) or increasing ALB of infrastructure to reflect daytime incoming radiation, which serves as an energy source for the nighttime SUHII.

I further investigate the intricate relationship between intracity LST variations and societal inequality. The significant contribution of this research lies in its exploration of how urban heat distribution correlates with social disparities within cities. The

insights gained are not just academically intriguing—they have profound implications for real-world applications. For instance, thermal discomfort, which can be caused by high LST, can lead to substantial health impacts (Lee and Dessler 2023). Populations with higher vulnerability often lack the necessary resources and access to effectively mitigate these potential impacts. This disparity underscores the importance of addressing environmental and social inequities in urban planning and public health initiatives. This aligns with critical social justice considerations in environmental research, highlighting areas where intervention can yield the most significant impact.

7. Limitations and future direction

While this study makes significant strides in understanding urban LST dynamics, it has limitations and potential avenues for enhancement. First, the inherent constraint of satellite measurements is that they capture only surface temperatures. Measures such as 2-m air temperature or wet-bulb temperature, which can have a more direct societal impact, are not accessible through this method.

Second, there is room for improvement in identifying potential drivers of seasonal and diurnal SUHI cycles, particularly those associated with nighttime seasonal variations. In this study, I utilize satellite-based estimates of EVI, ALB, and NL, along with reanalysis data of T2M and RH. However, as noted in the previous section and corroborated by earlier studies, pinpointing drivers of the nighttime seasonal cycle may require the incorporation of additional predictors. These include aspects of urban morphology (El Kenawy et al. 2020; Peng et al. 2022; Siddiqui et al. 2021), building orientation and materials (Farhadi et al. 2019; Okumus and Terzi 2021; Subramanian 2023), and further socioeconomic data (Best and Grimmond 2015; Feng et al. 2012; Ward et al. 2016), such as traffic patterns (Derdouri et al. 2021; H. Li et al. 2018). These factors could provide a more comprehensive understanding of the variables influencing the nighttime seasonal cycles of SUHI.

Third, it is notable that I employed the SVI to quantify population vulnerability, an index that integrates multiple factors influencing various vulnerabilities across the population. In future studies with a similar framework yet targeting specific outcomes related to heat, such as health, it is crucial to emphasize factors such as age or insurance coverage more significantly than the general SVI. Similarly, when the research objective centers on economic status, it is imperative to concentrate more on variables such as income or employment rates.

Last, the 2-km resolution offered by GOES satellites, though beneficial in terms of continuous monitoring, is coarser than that offered by some polar-orbiting satellites. This can pose challenges for a detailed intracity LST analysis, especially if the focus is neighborhood or block scale. In this study, I used SVI data, which are originally at the census tract level (around 4000 population), which is comparable with the GOES resolution of 2 km. However, for a detailed block-level analysis, LST with higher spatial resolution may be needed, whether from polar-orbiting satellites or through downscaling of LST estimates.

Acknowledgments. This material is based on work supported by the U.S. Department of Energy, Office of Science, Office of Biological and Environmental Research's Urban Integrated Field Laboratories' CROCUS Project research activity, under Award DE-SC0023226.

Data availability statement. All data used in this study are publicly available. GOES data used in this study are available in Amazon Web Services (AWS) repository. *GOES-16* data can be found at https://noaa-goes16.s3.amazonaws.com/index.html, and *GOES-17* data can be found at https://noaa-goes17.s3.amazonaws.com/index.html. ERA5 Land data are available on the Climate Data Store: https://doi.org/10.24381/cds.e2161bac. VIIRS datasets, including EVI, ALB, and NL, are available in the NASA Earthdata portal: https://www.earthdata.nasa.gov/. Gridded population data (GPW v4) are available in the NASA's Socioeconomic Data and Applications Center (SEDAC) archive: https://sedac.ciesin.columbia.edu/data/collection/gpw-v4. Gridded SVI data can also be found in SEDAC: https://sedac.ciesin.columbia.edu/data/set/usgrid-us-social-vulnerability-index.

REFERENCES

Bechtel, B., M. Demuzere, G. Mills, W. Zhan, P. Sismanidis, C. Small, and J. Voogt, 2019: SUHI analysis using local climate zones—A comparison of 50 cities. *Urban Climate*, **28**, 100451, https://doi.org/10.1016/j.uclim.2019.01.005.

Beck, C., and Coauthors, 2018: Air temperature characteristics of local climate zones in the Augsburg urban area (Bavaria, Southern Germany) under varying synoptic conditions. *Urban Climate*, **25**, 152–166, https://doi.org/10.1016/j.uclim.2018.04.007.

Best, M. J., and C. S. B. Grimmond, 2015: Key conclusions of the first international urban land surface model comparison project. *Bull. Amer. Meteor. Soc.*, **96**, 805–819, https://doi.org/10.1175/BAMS-D-14-00122.1.

Bindajam, A. A., J. Mallick, S. AlQadhi, C. K. Singh, and H. T. Hang, 2020: Impacts of vegetation and topography on land surface temperature variability over the semi-arid mountain cities of Saudi Arabia. *Atmosphere*, **11**, 762, https://doi.org/10.3390/atmos11070762.

Chakraborty, T., A. Hsu, D. Manya, and G. Sheriff, 2020: A spatially explicit surface urban heat island database for the United States: Characterization, uncertainties, and possible applications. *ISPRS J. Photogramm. Remote Sens.*, **168**, 74–88, https://doi.org/10.1016/j.isprsjprs.2020.07.021.

Chakraborty, T. C., X. Lee, S. Ermida, and W. Zhan, 2021: On the land emissivity assumption and Landsat-derived surface urban heat islands: A global analysis. *Remote Sens. Environ.*, **265**, 112682, https://doi.org/10.1016/j.rse.2021.112682.

Chang, Y., and Coauthors, 2021: Exploring diurnal cycles of surface urban heat island intensity in Boston with land surface temperature data derived from GOES-R geostationary satellites. *Sci. Total Environ.*, **763**, 144224, https://doi.org/10.1016/j.scitotenv.2020.144224.

——, J. Xiao, X. Li, D. Zhou, and Y. Wu, 2022: Combining GOES-R and ECOSTRESS land surface temperature data to investigate diurnal variations of surface urban heat island. *Sci. Total Environ.*, **823**, 153652, https://doi.org/10.1016/j.scitotenv.2022.153652.

de Almeida, C. R., A. C. Teodoro, and A. Gonçalves, 2021: Study of the Urban Heat Island (UHI) using remote sensing data/techniques: A systematic review. *Environments*, **8**, 105, https://doi.org/10.3390/environments8100105.

Deilami, K., M. Kamruzzaman, and Y. Liu, 2018: Urban heat island effect: A systematic review of spatio-temporal factors, data, methods, and mitigation measures. *Int. J. Appl. Earth Obs. Geoinf.*, **67**, 30–42, https://doi.org/10.1016/j.jag.2017.12.009.

Derdouri, A., R. Wang, Y. Murayama, and T. Osaragi, 2021: Understanding the links between LULC changes and SUHI in cities: Insights from two-decadal studies (2001–2020). *Remote Sens.*, **13**, 3654, https://doi.org/10.3390/rs13183654.

Doxsey-Whitfield, E., K. MacManus, S. B. Adamo, L. Pistolesi, J. Squires, O. Borkovska, and S. R. Baptista, 2015: Taking advantage of the improved availability of census data: A first look at the gridded population of the world, version 4. *Pap. Appl. Geogr.*, **1**, 226–234, https://doi.org/10.1080/23754931.2015.1014272.

Dutta, K., D. Basu, and S. Agrawal, 2022: Evaluation of seasonal variability in magnitude of urban heat islands using local climate zone classification and surface albedo. *Int. J. Environ. Sci. Technol.*, **19**, 8677–8698, https://doi.org/10.1007/s13762-021-03602-w.

El Kenawy, A. M., and Coauthors, 2020: Nocturnal surface urban heat island over Greater Cairo: Spatial morphology, temporal trends and links to land-atmosphere influences. *Remote Sens.*, **12**, 3889, https://doi.org/10.3390/rs12233889.

Farhadi, H., M. Faizi, and H. Sanaieian, 2019: Mitigating the urban heat island in a residential area in Tehran: Investigating the role of vegetation, materials, and orientation of buildings. *Sustainable Cities Soc.*, **46**, 101448, https://doi.org/10.1016/j.scs.2019.101448.

Feng, J.-M., Y.-L. Wang, Z.-G. Ma, and Y.-H. Liu, 2012: Simulating the regional impacts of urbanization and anthropogenic heat release on climate across China. *J. Climate*, **25**, 7187–7203, https://doi.org/10.1175/JCLI-D-11-00333.1.

Flanagan, B. E., E. W. Gregory, E. J. Hallisey, J. L. Heitgerd, and B. Lewis, 2011: A social vulnerability index for disaster management. *J. Homeland Secur. Emerg. Manage.*, **8**, 3, https://doi.org/10.2202/1547-7355.1792.

Goldblatt, R., A. Addas, D. Crull, A. Maghrabi, G. G. Levin, and S. Rubinyi, 2021: Remotely sensed derived land surface temperature (LST) as a proxy for air temperature and thermal comfort at a small geographical scale. *Land*, **10**, 410, https://doi.org/10.3390/land10040410.

Guha, S., and H. Govil, 2022: Seasonal impact on the relationship between land surface temperature and normalized difference vegetation index in an urban landscape. *Geocarto Int.*, **37**, 2252–2272, https://doi.org/10.1080/10106049.2020.1815867.

Hsu, A., G. Sheriff, T. Chakraborty, and D. Manya, 2021: Disproportionate exposure to urban heat island intensity across major US cities. *Nat. Commun.*, **12**, 2721, https://doi.org/10.1038/s41467-021-22799-5.

Hu, L., and N. A. Brunsell, 2013: The impact of temporal aggregation of land surface temperature data for Surface Urban Heat Island (SUHI) monitoring. *Remote Sens. Environ.*, **134**, 162–174, https://doi.org/10.1016/j.rse.2013.02.022.

Huang, X., and Y. Wang, 2019: Investigating the effects of 3D urban morphology on the surface urban heat island effect in urban functional zones by using high-resolution remote sensing data: A case study of Wuhan, Central China. *ISPRS J. Photogramm. Remote Sens.*, **152**, 119–131, https://doi.org/10.1016/j.isprsjprs.2019.04.010.

Imran, H. M., A. Hossain, A. K. M. Saiful Islam, A. Rahman, M. A. E. Bhuiyan, S. Paul, and A. Alam, 2021: Impact of land cover changes on land surface temperature and human thermal comfort in Dhaka City of Bangladesh. *Earth Syst. Environ.*, **5**, 667–693, https://doi.org/10.1007/s41748-021-00243-4.

Jin, K., F. Wang, and S. Wang, 2020: Assessing the spatiotemporal variation in anthropogenic heat and its impact on the surface thermal environment over global land areas. *Sustainable Cities Soc.*, **63**, 102488, https://doi.org/10.1016/j.scs.2020.102488.

Kaplan, G., U. Avdan, and Z. Y. Avdan, 2018: Urban heat island analysis using the Landsat 8 satellite data: A case study in Skopje, Macedonia. *Proceedings*, **2**, 358, https://doi.org/10.3390/ecrs-2-05171.

Krayenhoff, E. S., M. Moustaoui, A. M. Broadbent, V. Gupta, and M. Georgescu, 2018: Diurnal interaction between urban expansion, climate change and adaptation in US cities. *Nat. Climate Change*, **8**, 1097–1103, https://doi.org/10.1038/s41558-018-0320-9.

Lai, J., and Coauthors, 2021: Meteorological controls on daily variations of nighttime surface urban heat islands. *Remote Sens. Environ.*, **253**, 112198, https://doi.org/10.1016/j.rse.2020.112198.

Leconte, F., J. Bouyer, R. Claverie, and M. Pétrissans, 2015: Using local climate zone scheme for UHI assessment: Evaluation of the method using mobile measurements. *Build. Environ.*, **83**, 39–49, https://doi.org/10.1016/j.buildenv.2014.05.005.

——, ——, and ——, 2020: Nocturnal cooling in local climate zone: Statistical approach using mobile measurements. *Urban Climate*, **33**, 100629, https://doi.org/10.1016/j.uclim.2020.100629.

Lee, J., and A. E. Dessler, 2023: Future temperature-related deaths in the U.S.: The impact of climate change, demographics, and adaptation. *GeoHealth*, **7**, e2023GH000799, https://doi.org/10.1029%2F2023GH000799.

——, and ——, 2024: Improved surface urban heat impact assessment using GOES satellite data: A comparative study with ERA-5. *Geophys. Res. Lett.*, **51**, e2023GL107364, https://doi.org/10.1029/2023GL107364.

Li, H., F. Meier, X. Lee, T. Chakraborty, J. Liu, M. Schaap, and S. Sodoudi, 2018: Interaction between urban heat island and urban pollution island during summer in Berlin. *Sci. Total Environ.*, **636**, 818–828, https://doi.org/10.1016/j.scitotenv.2018.04.254.

Li, K., K. Guan, C. Jiang, S. Wang, B. Peng, and Y. Cai, 2021: Evaluation of four new Land Surface Temperature (LST) products in the U.S. Corn Belt: ECOSTRESS, GOES-R, Landsat, and Sentinel-3. *IEEE J. Sel. Top. Appl. Earth Obs. Remote Sens.*, **14**, 9931–9945, https://doi.org/10.1109/JSTARS.2021.3114613.

Li, L., Y. Zha, and R. Wang, 2020a: Relationship of surface urban heat island with air temperature and precipitation in global large cities. *Ecol. Indic.*, **117**, 106683, https://doi.org/10.1016/j.ecolind.2020.106683.

——, ——, and J. Zhang, 2020b: Spatially non-stationary effect of underlying driving factors on surface urban heat islands in

global major cities. *Int. J. Appl. Earth Obs. Geoinf.*, **90**, 102131, https://doi.org/10.1016/j.jag.2020.102131.

Li, X., Y. Zhou, G. R. Asrar, and Z. Zhu, 2018: Creating a seamless 1 km resolution daily land surface temperature dataset for urban and surrounding areas in the conterminous United States. *Remote Sens. Environ.*, **206**, 84–97, https://doi.org/10.1016/j.rse.2017.12.010.

Li, Z.-L., M. Si, and P. Leng, 2020: A review of remotely sensed surface urban heat islands from the fresh perspective of comparisons among different regions (invited review). *Prog. Electromagn. Res.*, **102C**, 31–46, https://doi.org/10.2528/PIERC20020403.

Liu, Z., and Coauthors, 2022: Taxonomy of seasonal and diurnal clear-sky climatology of surface urban heat island dynamics across global cities. *ISPRS J. Photogramm. Remote Sens.*, **187**, 14–33, https://doi.org/10.1016/j.isprsjprs.2022.02.019.

Manoli, G., S. Fatichi, E. Bou-Zeid, and G. G. Katul, 2020: Seasonal hysteresis of surface urban heat islands. *Proc. Natl. Acad. Sci. USA*, **117**, 7082–7089, https://doi.org/10.1073/pnas.1917554117.

Mentaschi, L., G. Duveiller, G. Zulian, C. Corbane, M. Pesaresi, J. Maes, A. Stocchino, and L. Feyen, 2022: Global long-term mapping of surface temperature shows intensified intra-city urban heat island extremes. *Global Environ. Change*, **72**, 102441, https://doi.org/10.1016/j.gloenvcha.2021.102441.

Ming, Y., Y. Liu, J. Gu, J. Wang, and X. Liu, 2023: Nonlinear effects of urban and industrial forms on surface urban heat island: Evidence from 162 Chinese prefecture-level cities. *Sustainable Cities Soc.*, **89**, 104350, https://doi.org/10.1016/j.scs.2022.104350.

Morabito, M., A. Crisci, G. Guerri, A. Messeri, L. Congedo, and M. Munafò, 2021: Surface urban heat islands in Italian metropolitan cities: Tree cover and impervious surface influences. *Sci. Total Environ.*, **751**, 142334, https://doi.org/10.1016/j.scitotenv.2020.142334.

Muñoz-Sabater, J., and Coauthors, 2021: ERA5-land: A state-of-the-art global reanalysis dataset for land applications. *Earth Syst. Sci. Data*, **13**, 4349–4383, https://doi.org/10.5194/essd-13-4349-2021.

Oke, T. R., 1982: The energetic basis of the urban heat island. *Quart. J. Roy. Meteor. Soc.*, **108** (455), 1–24, https://doi.org/10.1002/qj.49710845502.

——, G. Mills, A. Christen, and J. A. Voogt, 2017: *Urban Climates.* Cambridge University Press, 542 pp.

Okumus, D. E., and F. Terzi, 2021: Evaluating the role of urban fabric on surface urban heat island: The case of Istanbul. *Sustain. Cities Soc.*, **73**, 103128, https://doi.org/10.1016/j.scs.2021.103128.

Patel, S., M. Indraganti, and R. N. Jawarneh, 2024: A comprehensive systematic review: Impact of Land Use/Land Cover (LULC) on Land Surface Temperatures (LST) and outdoor thermal comfort. *Build. Environ.*, **249**, 111130, https://doi.org/10.1016/j.buildenv.2023.111130.

Peng, J., J. Ma, Q. Liu, Y. Liu, Y. Hu, Y. Li, and Y. Yue, 2018: Spatial-temporal change of land surface temperature across 285 cities in China: An urban-rural contrast perspective. *Sci. Total Environ.*, **635**, 487–497, https://doi.org/10.1016/j.scitotenv.2018.04.105.

Peng, W., R. Wang, J. Duan, W. Gao, and Z. Fan, 2022: Surface and canopy urban heat islands: Does urban morphology result in the spatiotemporal differences? *Urban Climate*, **42**, 101136, https://doi.org/10.1016/j.uclim.2022.101136.

Pereira, C. T., É. Masiero, and V. Bourscheidt, 2021: Socio-spatial inequality and its relationship to thermal (dis) comfort in two major local climate zones in a tropical coastal city. *Int. J. Biometeor.*, **65**, 1177–1187, https://doi.org/10.1007/s00484-021-02099-9.

Ramankutty, N., C. Delire, and P. Snyder, 2006: Feedbacks between agriculture and climate: An illustration of the potential unintended consequences of human land use activities. *Global Planet. Change*, **54**, 79–93, https://doi.org/10.1016/j.gloplacha.2005.10.005.

Rasul, A., H. Balzter, and C. Smith, 2016: Diurnal and seasonal variation of surface urban cool and heat islands in the semi-arid city of Erbil, Iraq. *Climate*, **4**, 42, https://doi.org/10.3390/cli4030042.

——, ——, ——, J. Remedios, B. Adamu, J. A. Sobrino, M. Srivanit, and Q. Weng, 2017: A review on remote sensing of urban heat and cool islands. *Land*, **6**, 38, https://doi.org/10.3390/land6020038.

Rogan, J., M. Ziemer, D. Martin, S. Ratick, N. Cuba, and V. DeLauer, 2013: The impact of tree cover loss on land surface temperature: A case study of central Massachusetts using Landsat thematic mapper thermal data. *Appl. Geogr.*, **45**, 49–57, https://doi.org/10.1016/j.apgeog.2013.07.004.

Rousta, I., M. O. Sarif, R. D. Gupta, H. Olafsson, M. Ranagalage, Y. Murayama, H. Zhang, and T. D. Mushore, 2018: Spatiotemporal analysis of land use/land cover and its effects on surface urban heat island using Landsat data: A case study of Metropolitan City Tehran (1988–2018). *Sustainability*, **10**, 4433, https://doi.org/10.3390/su10124433.

Sagris, V., and M. Sepp, 2017: Landsat-8 TIRS data for assessing urban heat island effect and its impact on human health. *IEEE Geosci. Remote Sens. Lett.*, **14**, 2385–2389, https://doi.org/10.1109/LGRS.2017.2765703.

Santágata, D. M., P. Castesana, C. E. Rössler, and D. R. Gómez, 2017: Extreme temperature events affecting the electricity distribution system of the metropolitan area of Buenos Aires (1971–2013). *Energy Policy*, **106**, 404–414, https://doi.org/10.1016/j.enpol.2017.04.006.

Sarafanov, M., E. Kazakov, N. O. Nikitin, and A. V. Kalyuzhnaya, 2020: A machine learning approach for remote sensing data gap-filling with open-source implementation: An example regarding land surface temperature, surface albedo and NDVI. *Remote Sens.*, **12**, 3865, https://doi.org/10.3390/rs12233865.

Sarif, M. O., B. Rimal, and N. E. Stork, 2020: Assessment of changes in land use/land cover and land surface temperatures and their impact on surface urban heat island phenomena in the Kathmandu Valley (1988–2018). *ISPRS Int. J. Geo-Inf.*, **9**, 726, https://doi.org/10.3390/ijgi9120726.

Shao, L., W. Liao, P. Li, M. Luo, X. Xiong, and X. Liu, 2023: Drivers of global surface urban heat islands: Surface property, climate background, and 2D/3D urban morphologies. *Build. Environ.*, **242**, 110581, https://doi.org/10.1016/j.buildenv.2023.110581.

Shen, J., A. Huete, N. N. Tran, R. Devadas, X. Ma, D. Eamus, and Q. Yu, 2018: Diverse sensitivity of winter crops over the growing season to climate and land surface temperature across the rainfed cropland-belt of eastern Australia. *Agric. Ecosyst. Environ.*, **254**, 99–110, https://doi.org/10.1016/j.agee.2017.11.023.

Shi, H., G. Xian, R. Auch, K. Gallo, and Q. Zhou, 2021: Urban heat island and its regional impacts using remotely sensed thermal data—A review of recent developments and methodology. *Land*, **10**, 867, https://doi.org/10.3390/land10080867.

Shiff, S., D. Helman, and I. M. Lensky, 2021: Worldwide continuous gap-filled MODIS land surface temperature dataset. *Sci. Data*, **8**, 74, https://doi.org/10.1038/s41597-021-00861-7.

Siddiqui, A., G. Kushwaha, B. Nikam, S. K. Srivastav, A. Shelar, and P. Kumar, 2021: Analysing the day/night seasonal and annual changes and trends in land surface temperature and Surface Urban Heat Island Intensity (SUHII) for Indian cities. *Sustain. Cities Soc.*, **75**, 103374, https://doi.org/10.1016/j.scs.2021.103374.

Sidiqui, P., A. Huete, and R. Devadas, 2016: Spatio-temporal mapping and monitoring of urban heat island patterns over Sydney, Australia using MODIS and Landsat-8. *2016 Fourth Int. Workshop on Earth Observation and Remote Sensing Applications (EORSA)*, Guangzhou, China, Institute of Electrical and Electronics Engineers, 217–221, https://doi.org/10.1109/EORSA.2016.7552800.

Stone, B., Jr., and Coauthors, 2021: Compound climate and infrastructure events: How electrical grid failure alters heat wave risk. *Environ. Sci. Technol.*, **55**, 6957–6964, https://doi.org/10.1021/acs.est.1c00024.

Subramanian, S., 2023: Thermal performance study of building materials in an urban form. *IOP Conf. Ser.: Earth Environ. Sci.*, **1210**, 012038, https://doi.org/10.1088/1755-1315/1210/1/012038.

Tetali, S., N. Baird, and K. Klima, 2022: A multicity analysis of daytime surface urban heat islands in India and the US. *Sustain. Cities Soc.*, **77**, 103568, https://doi.org/10.1016/j.scs.2021.103568.

Tomlinson, C. J., L. Chapman, J. E. Thornes, and C. J. Baker, 2012: Derivation of Birmingham's summer surface urban heat island from MODIS satellite images. *Int. J. Climatol.*, **32**, 214–224, https://doi.org/10.1002/joc.2261.

Wang, C., S. W. Myint, Z. Wang, and J. Song, 2016: Spatio-temporal modeling of the urban heat island in the Phoenix metropolitan area: Land use change implications. *Remote Sens.*, **8**, 185, https://doi.org/10.3390/rs8030185.

——, A. Middel, S. W. Myint, S. Kaplan, A. J. Brazel, and J. Lukasczyk, 2018: Assessing local climate zones in arid cities: The case of Phoenix, Arizona and Las Vegas, Nevada. *ISPRS J. Photogramm. Remote Sens.*, **141**, 59–71, https://doi.org/10.1016/j.isprsjprs.2018.04.009.

Wang, L., and D. Li, 2021: Urban heat islands during heat waves: A comparative study between Boston and Phoenix. *J. Appl. Meteor. Climatol.*, **60**, 621–641, https://doi.org/10.1175/JAMC-D-20-0132.1.

Wang, Y.-C., B. K. H. Hu, S. W. Myint, C.-C. Feng, W. T. L. Chow, and P. F. Passy, 2018: Patterns of land change and their potential impacts on land surface temperature change in Yangon, Myanmar. *Sci. Total Environ.*, **643**, 738–750, https://doi.org/10.1016/j.scitotenv.2018.06.209.

Wang, Z., Q. Meng, M. Allam, D. Hu, L. Zhang, and M. Menenti, 2021: Environmental and anthropogenic drivers of surface urban heat island intensity: A case-study in the Yangtze River Delta, China. *Ecol. Indic.*, **128**, 107845, https://doi.org/10.1016/j.ecolind.2021.107845.

Wang, Z.-H., and Q. Li, 2017: Thermodynamic characterisation of urban nocturnal cooling. *Heliyon*, **3**, e00290, https://doi.org/10.1016/j.heliyon.2017.e00290.

Ward, K., S. Lauf, B. Kleinschmit, and W. Endlicher, 2016: Heat waves and urban heat islands in Europe: A review of relevant drivers. *Sci. Total Environ.*, **569–570**, 527–539, https://doi.org/10.1016/j.scitotenv.2016.06.119.

Wickham, J. D., T. G. Wade, and K. H. Riitters, 2012: Comparison of cropland and forest surface temperatures across the conterminous United States. *Agric. For. Meteor.*, **166–167**, 137–143, https://doi.org/10.1016/j.agrformet.2012.07.002.

Wong, M. S., F. Peng, B. Zou, W. Z. Shi, and G. J. Wilson, 2016: Spatially analyzing the inequity of the Hong Kong urban heat island by socio-demographic characteristics. *Int. J. Environ. Res. Public Health*, **13**, 317, https://doi.org/10.3390/ijerph13030317.

Wu, S., W. Yu, and B. Chen, 2023: Observed inequality in thermal comfort exposure and its multifaceted associations with greenspace in United States cities. *Landscape Urban Plann.*, **233**, 104701, https://doi.org/10.1016/j.landurbplan.2023.104701.

Yang, X., and L. Yao, 2022: Reexamining the relationship between surface urban heat island intensity and annual precipitation: Effects of reference rural land cover. *Urban Climate*, **41**, 101074, https://doi.org/10.1016/j.uclim.2021.101074.

Yang, Y., and Coauthors, 2020: Modulations of surface thermal environment and agricultural activity on intraseasonal variations of summer diurnal temperature range in the Yangtze River Delta of China. *Sci. Total Environ.*, **736**, 139445, https://doi.org/10.1016/j.scitotenv.2020.139445.

Yao, R., L. Wang, X. Huang, Y. Niu, Y. Chen, and Z. Niu, 2018: The influence of different data and method on estimating the surface urban heat island intensity. *Ecol. Indic.*, **89**, 45–55, https://doi.org/10.1016/j.ecolind.2018.01.044.

——, ——, ——, W. Gong, and X. Xia, 2019: Greening in rural areas increases the surface urban heat island intensity. *Geophys. Res. Lett.*, **46**, 2204–2212, https://doi.org/10.1029/2018GL081816.

Yin, Y., L. He, P. O. Wennberg, and C. Frankenberg, 2023: Unequal exposure to heatwaves in Los Angeles: Impact of uneven green spaces. *Sci. Adv.*, **9**, eade8501, https://doi.org/10.1126/sciadv.ade8501.

Yu, Y., and P. Yu, 2020: Land surface temperature product from the GOES-R series. *The GOES-R Series*, J. Steven et al., Eds., Elsevier, 133–144.

——, D. Tarpley, J. L. Privette, M. D. Goldberg, M. K. R. V. Raja, K. Y. Vinnikov, and H. Xu, 2008: Developing algorithm for operational GOES-R land surface temperature product. *IEEE Trans. Geosci. Remote Sens.*, **47**, 936–951, https://doi.org/10.1109/TGRS.2008.2006180.

Yuan, B., and Coauthors, 2023: Global distinct variations of surface urban heat islands in inter-and intra-cities revealed by local climate zones and seamless daily land surface temperature data. *ISPRS J. Photogramm. Remote Sens.*, **204**, 1–14, https://doi.org/10.1016/j.isprsjprs.2023.08.012.

Yuan, Y., C. Li, X. Geng, Z. Yu, Z. Fan, and X. Wang, 2022: Natural-anthropogenic environment interactively causes the surface urban heat island intensity variations in global climate zones. *Environ. Int.*, **170**, 107574, https://doi.org/10.1016/j.envint.2022.107574.

Zanaga, D., and Coauthors, 2022: ESA WorldCover 10 m 2021 v200. Accessed 1 August 2023, https://doi.org/10.5281/zenodo.7254221.

Zhang, Z., and Q. Du, 2022: Hourly mapping of surface air temperature by blending geostationary datasets from the two-satellite system of GOES-R series. *ISPRS J. Photogramm. Remote Sens.*, **183**, 111–128, https://doi.org/10.1016/j.isprsjprs.2021.10.022.

Zhou, D., S. Zhao, S. Liu, L. Zhang, and C. Zhu, 2014: Surface urban heat island in China's 32 major cities: Spatial patterns and drivers. *Remote Sens. Environ.*, **152**, 51–61, https://doi.org/10.1016/j.rse.2014.05.017.

Zhou, L., B. Yuan, F. Hu, C. Wei, X. Dang, and D. Sun, 2022: Understanding the effects of 2D/3D urban morphology on land surface temperature based on local climate zones. *Build. Environ.*, **208**, 108578, https://doi.org/10.1016/j.buildenv.2021.108578.